Scilight

Regenerative Medicine and Dentistry
https://www.sciltp.com/journals/rmd

Article

Mandibular Periosteal Cells Exhibit *Trpv2*-Dependent Mechanosensitivity to Microscale Stiffness Patterns

Qianying Lin [1,†], Conghui Zhang [1,†], Kaijie Zhang [2], Siyu Jin [1], Longjian Xue [2,*] and Wei Ji [1,3,*]

[1] State Key Laboratory of Oral & Maxillofacial Reconstruction and Regeneration, Key Laboratory of Oral Biomedicine Ministry of Education, Hubei Key Laboratory of Stomatology, School & Hospital of Stomatology, Wuhan University, Wuhan 430079, China
[2] School of Power and Mechanical Engineering, The Institute of Technological Science, Wuhan University, South Donghu Road 8, Wuhan 430072, China
[3] Department of Oral Implantology, School and Hospital of Stomatology, Wuhan University, Luoyu Road 237, Wuhan 430079, China
* Correspondence: xuelongjian@whu.edu.cn (L.X.); wei.ji@whu.edu.cn (W.J.)
† These authors contributed equally to this work.

How To Cite: Lin, Q.; Zhang, C.; Zhang, K.; et al. Mandibular Periosteal Cells Exhibit *Trpv2*-Dependent Mechanosensitivity to Microscale Stiffness Patterns. *Regenerative Medicine and Dentistry* **2026**, *3*(2), 9. https://doi.org/10.53941/rmd.2026.100009

Received: 1 April 2026
Revised: 18 May 2026
Accepted: 26 May 2026
Published: 16 June 2026

Abstract: The clinical need for maxillofacial reconstruction requires a deeper understanding of site-specific skeletal stem cell biology. The periosteum serves as a critical reservoir of adult skeletal stem progenitor cells (SSPCs) that navigate microscale stiffness gradients during bone healing. However, whether periosteal SSPCs from distinct skeletal sites exhibit divergent mechanosensitive responses remains poorly understood. This study compared the phenotypic characteristics and mechanotactic behaviors of mouse periosteal SSPCs (passage 3) from mandible (m-pSSPCs) and long bone (l-pSSPCs). Furthermore, we evaluated cell migration and adhesion using our previously reported flat PDMS substrate with periodic subsurface stiffness patterns (20-μm or 50-μm periods; stiffness differentials of ~0.3 MPa and ~0.5 MPa, respectively). While both cell types exhibited similar basal morphologies, flowcytometry and western blot analysis revealed a significantly higher proportion of osteogenic progenitors in m-pSSPCs compared to l-pSSPCs. Notably, m-pSSPCs displayed scale-dependent directional migration, morphological elongation and alignment exclusively on 50-μm patterns, whereas l-pSSPCs remained unresponsive across all scales. Transcriptomic profiling identified a marked enrichment of calcium-channel genes in m-pSSPCs, with *Trpv2* significantly upregulated. Selective *Trpv2* silencing abolished the characteristic polarization and alignment of m-pSSPCs on 50-μm stiffness patterns. Our findings demonstrate that m-pSSPCs possess a unique, *Trpv2*-dependent sensitivity to microscale mechanical cues, revealing site-specific mechanosensing programs in skeletal progenitors. These results highlight the necessity of considering tissue-specific cellular programs when designing "instructive" biomaterials for craniofacial regeneration.

Keywords: mechanosensitivity; periosteal cells; skeletal stem progenitor cells; microscale stiffness; *Trpv2*

1. Introduction

Mandibular bone defects caused by trauma, infection, and tumor resection pose significant clinical challenges, often severely compromising both patients' aesthetics and essential functional such as mastication, and

speech [1]. While autologous bone grafting remains the gold standard for reconstruction, its clinical efficacy is frequently constrained by donor site morbidity, infection risks, and unpredictable graft integration [2,3]. In East Asia alone, more than one million patients develop jawbone defects secondary to facial fractures [4]. Hence, effective and site-specific regenerative strategies grounded in a deep understanding of the underlying biological mechanisms are urgently needed.

The periosteum serves as a critical reservoir of adult skeletal stem/progenitor cells (SSPCs) essential for bone repair [5,6]. Following injury, periosteal SSPCs (pSSPCs) migrate to the defect site, where their behavior is governed by the local mechanical microenvironment [5,7–9]. During the healing process, the extracellular matrix (ECM) undergoes a dynamic stiffening transition from a soft callus to rigid bone, presenting SSPCs with a complex landscape of microscale stiffness gradients that guide cell polarization and directional migration [10–14]. Mechanosensitive ion channels, such as Piezo1 and TRP families, act as primary transducers that convert mechanical stimuli into intracellular chemical signals to regulate cell fate [15,16].

Despite these insights, significant knowledge gaps exist regarding the mechanosensing potentials of pSSPCs. First, pSSPCs derived from mandible (m-pSSPCs) and long bone (l-pSSPCs) display significantly biological characteristics: l-pSSPCs (mesoderm-derived) tend to proliferate faster, whereas m-pSSPCs (neural crest-derived) exhibit more rapid osteogenic differentiation, stronger mineralization, and superior *in vivo* bone regeneration [17,18]. These differences are likely attributable to their distinct embryological origins, histological architecture (such as collagen alignment and vascularization), and daily mechanical loading patterns [19]. Second, most mechanosensing studies utilize substrates of uniform stiffness, failing to recapitulate the anisotropic, gradient-rich mechanical interface cells encounter *in vivo* [20]. Hence, it remains largely unknown whether m-pSSPCs) and l-pSSPCs interpret and respond to identical microscale stiffness patterns in the same manner. Furthermore, the specific biological mechanism underlying site-specific mechanosensitivity in mandible versus appendicular skeleton progenitors remains unexplored.

In this study, we hypothesized that m-pSSPCs and l-pSSPCs possess distinct mechanosensitive capabilities when navigating microscale stiffness patterns. To test this, we engineered a polydimethylsiloxane (PDMS) platform featuring cellular-scale (20 or 50 μm) stiffness patterns. We compared the cell migration and adhesion of m-pSSPCs and l-pSSPCs on these substrates and investigated the underlying molecular mechanisms. Our findings reveal that m-pSSPCs display a unique, scale-dependent mechanosenstivity to 50 μm stiffness patterns, leading to enhanced alignment and directional migration, mediated by the elevated expression of *Trpv2* ion channels. This work not only uncovers the site-specific mechanobiology of periosteal cells but also suggests that *Trpv2* could be a pivotal target for designing smart and location-aware biomaterials for craniofacial regeneration and reconstruction.

2. Materials and Methods

2.1. Isolation and Expansion of Mouse m-pSSPCs and l-pSSPCs

Mouse m-pSSPCs and l-pSSPCs were harvested from 6–8 weeks old C57/BL mice and expanded them in vitro with growth medium (αMEM (Hyclone, SH30265.02) supplemented with 10% FBS (Gibco, SV30208.02) and 1% penicillin/streptomycin (Gibco, SV30208.02)) at 37 °C with 5% CO_2 according to previous study [18,21]. To obtain a sufficient number of primary cells, mandibles and femurs from 4 to 6 mice were pooled for each independent preparation. For RNA sequencing (RNA-seq), two independent pools were generated, resulting in two biological replicates at the pool level (n = 2). Cells were passaged when reaching 80% confluency with 0.25% trypsin (Hyclone, SH30236.02) and cells at passage 3 were used for further experiments.

2.2. Flowcytometry of In Vitro Cultured m-pSSPCs and l-pSSPCs

Subpopulation analysis using the cocktails of established skeletal stem/progenitor cell surface markers (CD51, CD90, CD105, 6C3, CD200, CD51, and CD31/45) were performed according to previously established protocol [21,22]. Flowcytometry analysis was subsequently performed using CytoFLEX Flow Cytometer (Beckman Coulter, Miami, FL, USA) and analyzed using FlowJo software with the Fluorescence Minus One (FMO) control as reference for appropriate gate choosing.

2.3. Western Blotting

The total proteins were harvested by lysis buffer (Merck Millipore, Billerica, MA, USA) with 1 × complete protease inhibitor (Roche) at 4 °C and then lysed supersonically. After centrifugation for 10 min with 13,000 rpm at 4 °C, the supernatant was collected, mixed with 5 × SDS-PAGE Protein Sampling Buffer (Biosharp, Hefei, China, BL521A) and denatured at 95 °C for 10 min. For each sample, 15 μg of denatured protein per well were

loaded onto an 10% polyacrylamide gel, separated by electrophoresis, and then transferred onto nitrocellulose membranes (Merck Millipore). After blocking by 5% skimmed milk for 1 h at room temperature, the membranes were incubated with the primary antibodies at 4 °C overnight as follows: RUNX2 (D1L7F, 1:1000, Cell Signaling Technology), and GAPDH (60004-1-Ig, 1:5000, Proteintech, Wuhan, China). The membranes were washed with TBST and incubated with a secondary antibody (ANT015 and ANT016, 1:2000, AntGene, Wuhan, China). After washes with TBST, the membranes were observed by WesternBright ECL HRP substrate (Advansta, San Jose, CA, USA K-12045).

2.4. Design and Characterization of Microscale Stiffness Cell Culture Substrate

A bilayer PDMS substrate with two different microscale stiffness pattern (20-μm and 50-μm patterns) were fabricated using soft lithography technique according to our previously reported protocol [23]. Prior to cell seeding, the substrate is activated with oxygen plasma and coated with poly-D-lysine (0.01 mg/mL) at 37 °C for 4 h. After that, the substrate was rinsed with Milli-Q water three times and air dried before further scanning electron microscopy (SEM) and atomic force microscopy (AFM) as previous protocol [23]. Plasma activation, PDL coating, and washing were applied simultaneously to the whole substrate to ensure the identical surface chemistry.

2.5. Cell Seeding and Live Imaging Analysis

Passage 3 of m-pSSPCs and l-pSSPCs were seeded at a density of 5000 cells/cm^2 on the PDL-coated microcale stiffness cell culture substrate placed in 24-well plate. Cells were cultured in growth medium and incubated in a High-Content Imaging System (PerkinElmer, Opera Phenix Plus, Buckinghamshire, UK) at 37 °C with 5% CO_2 for 16 h. Bright-field images were automatically acquired at 5-min intervals. Image sequences were imported into ImageJ software (version 1.54p, National Institutes of Health, Bethesda, MD, USA), and only non-contacting, non-proliferating cells were included for the migration analysis. Manual Tracking plugin was used to manually track cell migration trajectories, and to generate data of migration velocity and total path length. At least 25 cells from each sample were analyzed for migration velocity and positional data. Migration angles were binned in 5° intervals (36 bins from 0° to 180°) and fitted using a Gauss model. Migration efficiency (*M_eff*) was calculated as net displacement over total path length [24].

2.6. Immunofluorescence Staining and Imaging Analysis

After 16 h of culture, samples (n = 3 per group) were fixed with 4% paraformaldehyde for 10 min and permeabilized with 0.5% Triton X-100. Following three 5-min washes with PBS, cells were blocked with 5% normal donkey serum for 1 h at room temperature. For vinculin and F-actin co-staining, cells were incubated with anti-vinculin (66305-1-Ig, 1:300, Proteintech) overnight at 4 °C, washed three times with PBS (5 min each), and then incubated with Alexa Fluor 488 conjugated secondary antibody (ANT023, 1:200, AntGene) for 1 h at room temperature in the dark. For F-actin-only staining, the above vinculin antibody steps were omitted. Subsequently, all samples were stained with phalloidin (YP0052L, UElandy, Suzhou, China). The phalloidin stock solution (200 tests/mL) was diluted 1:500 in PBS prior to use, and samples were incubated for 20 min at room temperature, washed three times with PBS, and counterstained with DAPI. Images were acquired using a confocal microscope (OLYMPUS FV3000) and processed with the Fiji image analysis package. For morphology, images were taken at 10× magnification, and >90 cells per group were analyzed. Cell migration was tracked manually using the "Manual Tracking" plugin. Following thresholding, an ellipse was fitted to each cell to determine cell size and axis ratio (AR). For vinculin quantification, images were taken at 60× magnification and analyzed following the workflow described in Horzum et al. [25]. For each group, 13–19 cells were manually selected for analysis based on their location on the stiff and soft regions.

2.7. RNA Sequencing (RNA Seq) and Data Analysis

Total RNA was extracted using the EZNA HP Total RNA Kit (Omega Bio-Tek, Norcross, GA, USA, R6812-02). RNA integrity and concentration were assessed using an Agilent 2100 Bioanalyzer (Agilent Technologies, Santa Clara, CA, USA). RNA sequencing was performed by the Beijing Genomics Institute (BGI, Shenzhen, China). Sequencing libraries were prepared as single-stranded circular DNA and sequenced on the DNBSEQ platform. Raw sequencing reads were processed using SOAPnuke to obtain clean reads. The clean reads were aligned to the mouse reference transcriptome using Bowtie2 [26], and gene expression levels were quantified using RSEM [27]. Differential expression analysis was conducted with DESeq2 [28], comparing l-pSSPCs versus m-pSSPCs. Significantly differentially expressed genes (DEGs) were defined as those with an absolute log2 fold

change (|log2FC|) > 1 and an adjusted *p*-value (padj) < 0.05. Visualization of results, including volcano plots, Gene Set Enrichment Analysis (GSEA), and heatmaps, was performed using R software (version 4.5.0, R Core Team, 2025, R Foundation for Statistical Computing, Vienna, Austria).

2.8. siRNA Transfection

For transient knockdown of *Trpv2*, mouse m-pSSPCs (passage 2) were transfected using Lipofectamine 2000 (Invitrogen, Carlsbad, CA, USA, 11668030). A *Trpv2*-targeting siRNA (si-*Trpv2*) and a non-targeting control siRNA (si-NC), both obtained from GenePharma (Shanghai, China) were used. The duplex sequence for si-*Trpv2* was: sense strand 5′-GGUAGAGAAUGGAGCGAAUTT-3′ and antisense strand 5‘-AUUCGCUCCAUUCUCUACCTT-3′. Following the manufacturer’s protocol, the siRNA and Lipofectamine 2000 were separately diluted in Opti-MEM Reduced Serum Medium (Gibco, Waltham, MA, USA, 31985062) and then combined to form transfection complexes. At 8 h post-transfection, the cells were trypsinized and seeded on the microscale stiffness cell culture substrate for the aforementioned migration analysis and immunofluorescent staining.

2.9. Quantitative Reverse Transcription PCR

Total RNA was extracted from cells using the EZNA HP Total RNA Kit (Omega, Biel/Bienne, Switzerland, R6812-02), and reverse transcription was performed with the HiScript III All-in-one RT SuperMix (Vazyme, Nanjing, Jiangsu, China, R222). Quantitative real-time PCR (qRT-PCR) was conducted using the HiScript II One Step qRT-PCR SYBR Green Kit (Vazyme, Nanjing, China, Q711) on a CFX Connect Real-Time System (Bio-Rad, 1855201). The primers used in this study are listed in Table S1 (Sangon Biotech, Shanghai, China). *Gapdh* was used as the housekeeping gene for normalizing gene expression, and the relative expression levels of target genes were calculated using the $2^{-\Delta\Delta Ct}$ method.

2.10. Statistical Analysis

For all experiments, cells at passage 3 were assayed in triplicate (n = 3). In each sample, at least three randomly selected fields were imaged for further analysis. All the numerical data were represented as mean ± SD, and data are plotted as individual data points with bars representing the average value. Statistical analysis and data visualization were performed using GraphPad Prism version 9 (La Jolla, CA, USA) and OriginPro 2025b (Northampton, MA, USA). Shapiro–Wilk test was used to test for normal distribution. Analysis of variance (ANOVA) with a Tukey post hoc test was used for multiple group experiments. Statistical significance was denoted on all tables and graphs as follows: * $p < 0.05$, ** $p < 0.01$, *** $p < 0.001$, **** $p < 0.0001$.

3. Results

3.1. Phenotypic Characterization of m-pSSPCs and l-pSSPCs

We harvested m-pSSPCs and l-pSSPCs from the same animals and expanded them in vitro at passage 3 (Figure 1A). Subpopulation analysis using established skeletal stem/progenitor cell markers revealed that both m-pSSPCs and l-pSSPCs at passage 3 were predominantly composed of osteogenic progenitors and pre-BCSPs [22] (Figure 1B, Table 1). Notably, m-pSSPCs contained a significantly higher proportion of osteogenic progenitors (54.6% vs. 35.2%, $p = 0.0003$), while l-pSSPCs harbored more mSSCs (5.9% vs. 0.3%, $p < 0.0001$) and pre-BCSPs (20.3% vs. 9.1%, $p < 0.0001$) (Table 1). Despite these compositional differences, both cell types exhibited similar polygonal morphologies and comparable cell sizes (Figure 1C). However, m-pSSPCs demonstrated higher baseline expression level of RUNX2 compared to the l-pSSPCs (Figure 1D). Together, these results indicate that while m-pSSPCs and l-pSSPCs at passage 3 remain highly similar morphology, they exhibit distinct cellular composition and osteogenic lineage priming, as evidenced by their divergent subpopulation distributions and RUNX2 expression.

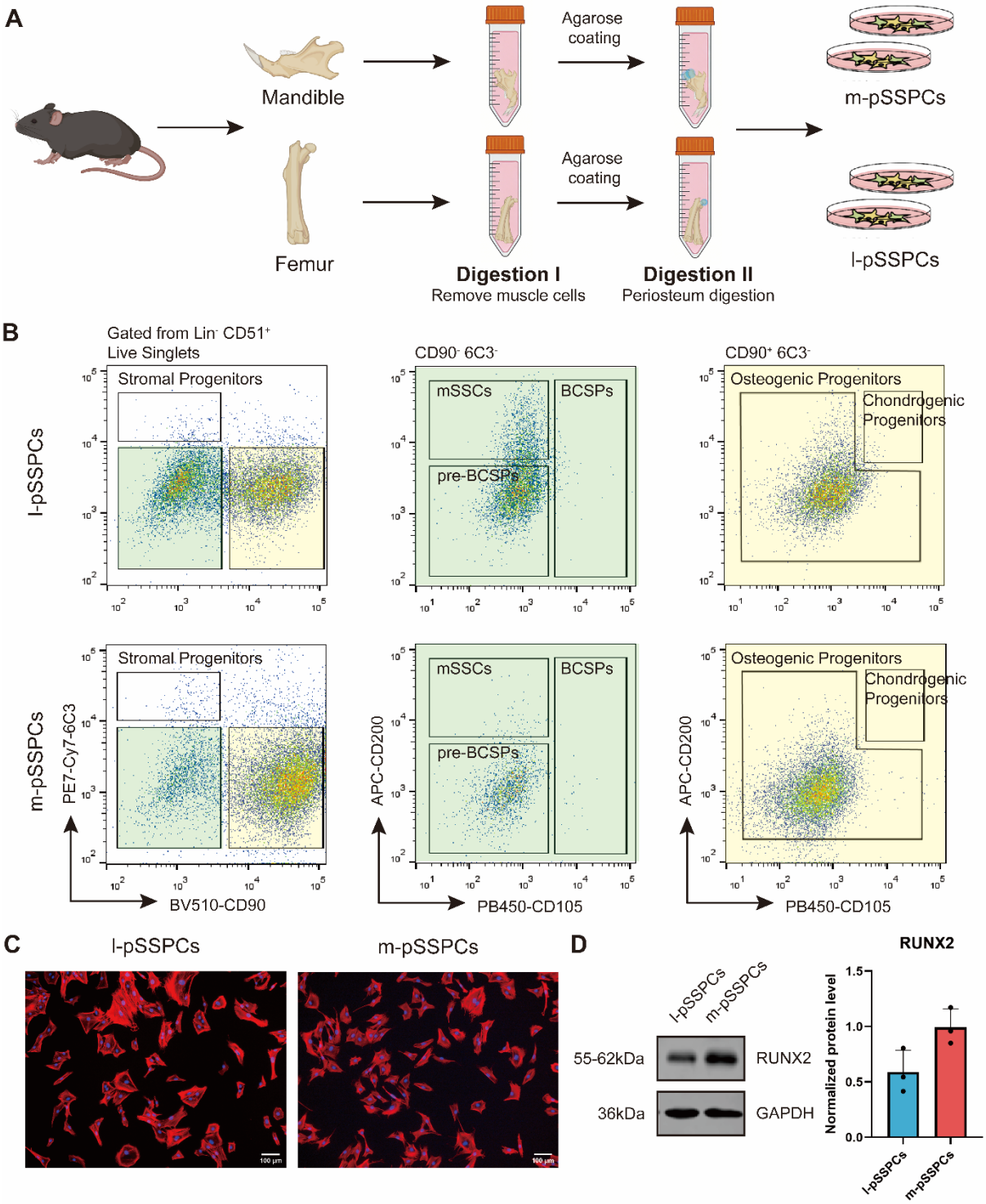

Figure 1. Baseline characterization of m-pSSPCs and l-pSSPCs. (**A**) Experimental workflow for cell isolation. Created with BioRender.com. (**B**) Flow cytometry plots showing the gating strategy and percentages of mouse skeletal stem cells (mSSCs), pre-BCSPs, BCSPs, osteogenic progenitors, chondrogenic progenitors, and stromal progenitors in m-pSSPCs and l-pSSPCs at passage 3. (**C**) Representative images of cytoskeleton staining of m-pSSPCs and l-pSSPCs. Scale bar, 100 μm. (**D**) Western blotting analysis and densitometry of RUNX2 in m-pSSPCs and l-pSSPCs at passage 3. Triplicate samples (n = 3) were used in each group.

Table 1. Flowcytometry analysis of l-pSSPCs and m-pSSPCs at passages 3.

Subpopulation Analysis	l-pSSPCs (mean ± SD)%	m-pSSPCs (mean ± SD)%	*p*-Value
mSSCs ($CD31^-CD45^-CD51^+CD90^-6C3^-CD105^-CD200^+$)	5.87 ± 0.23	0.31 ± 0.03	<0.0001
pre-BCSPs ($CD31^-CD45^-CD51^+CD90^-6C3^-CD105^-CD200^-$)	20.31 ± 0.3	9.09 ± 0.27	<0.0001
BCSPs ($CD31^-CD45^-CD51^+CD90^-6C3^-CD105^+$)	0.33 ± 0.02	0.11 ± 0.02	<0.0001
Osteogenic progenitors ($CD31^-CD45^-CD51^+CD90^+6C3^-CD105^+CD200^-$ or $CD31^-CD45^-CD51^+CD90^+6C3^-CD105^-$)	35.24 ± 0.31	54.6 ± 0.28	0.0003
Chondrogenic progenitors ($CD31^-CD45^-CD51^+CD90^+6C3^-CD105^+CD200^+$)	0.13 ± 0.02	0.01 ± 0.01	<0.0001
Stromal progenitors ($CD31^-CD45^-CD51^+CD90^-6C3^+$)	0.68 ± 0.01	0.8 ± 0.1	0.0897

3.2. Design and Characterization of Biomimetic Microscale Stiffness Substrates

To mimic the microscale mechanical heterogeneity of the in vivo healing interface, we developed a bilayer poly-D lysine coated PDMS substrate exhibiting spatially defined stiffness patterns. Scanning electron microscopy revealed a uniform soft top film (~9 μm thick, elastic modulus ~899 kPa,) suspended over a microfabricated ridge and groove structure made of stiff PDMS. (Figure 2A,B). Atomic force microscopy confirmed the presence of distinct stiff and soft regions corresponding to the underlying pattern. On the 50-μm-patterned substrate, the apparent elastic moduli (*E_app*) were ~2.4 MPa over the stiff ridges and ~1.9 MPa over the soft grooves, creating a stiffness differential of ~0.5 MPa (Figure 2C). A similar though slightly smaller, differential (~0.3 MPa) was observed on the 20-μm-patterned substrate, with the *E_app* of ~2.4 MPa and ~2.1 MPa for the stiff and soft regions, respectively (Figure 2D). These substrates thus provide a well-defined flat surface that recapitulates physiologically relevant mechanical heterogeneity at the microscale.

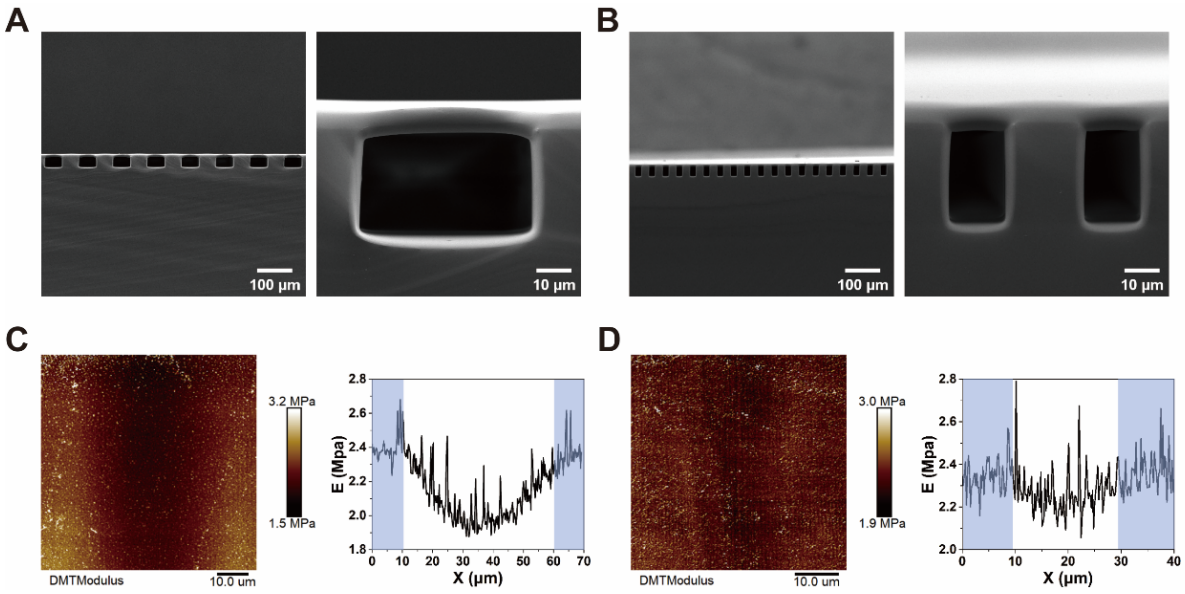

Figure 2. Topological morphology and stiffness distribution of the bilayer PDMS substrate. (**A**,**B**) Scanning electron microscopy images showing cross-sectional views of the uniform soft top film suspended over the microfabricated ridge and groove structure on substrates with 50-μm (**A**) and 20-μm (**B**) pattern periods. Scale bar, 100 μm and 10 μm. (**C**,**D**) Atomic force microscopy mapping of the apparent elastic modulus on the 50-μm-patterned (**C**) and 20-μm-patterned (**D**) substrates. Scale bar, 10 μm.

3.3. m-pSSPCs, but Not l-pSSPCs, Display Scale-Dependent Directional Migration on Stiffness Patterns

We next investigated the migratory responses of m-pSSPCs and l-pSSPCs to the stiffness patterns over 16 h. Overall, m-pSSPCs migrated at a lower overall velocity than l-pSSPCs on both 20-μm and 50-μm stiffness patterns (Figure 3B). Specifically, the m-pSSPCs exhibited pronounced scale dependent directional migration. On the

50-μm-patterned substrates, the m-pSSPCs displayed pronounced migration trajectories along the axis of the stiffness pattern, whereas their migration on the 20-μm-patterned substrates was largely random (Figure 3A). Quantitatively, this behavior was reflected by a significantly higher migration efficiency (*M_eff*)—calculated as net displacement over total path length—on the 50-μm pattern (*M_eff* = 0.23) compared to the 20-μm pattern (*M_eff* = 0.13) (Figure 3C). Conversely, l-pSSPCs did not show evident directional migration with isotropic trajectories on both 20-μm and 50-μm stiffness-patterned substrates (Figure 3A,C). Taken together, our data revealed a site-specific and scale-dependent mechanoresponse: m-pSSPCs possess a unique capacity to migrate along 50-μm stiffness patterns, a mechanical cue to which l-pSSPCs appear fundamentally insensitive.

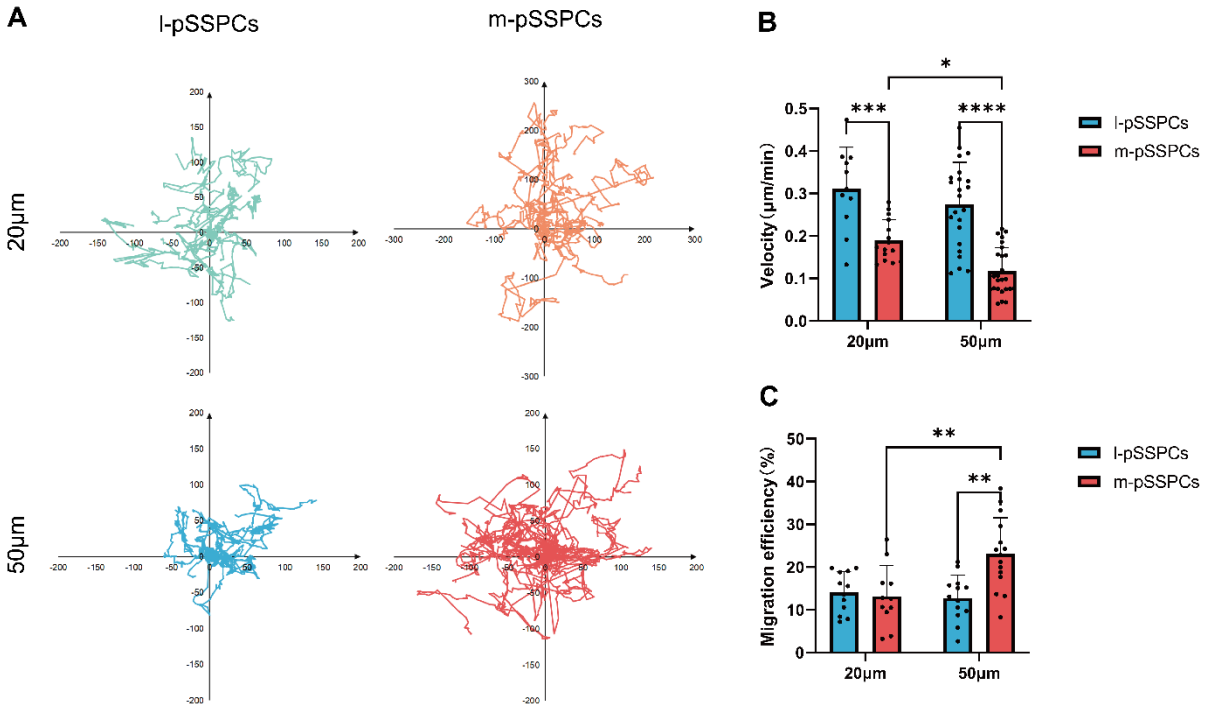

Figure 3. Scale-dependent directional migration of m-pSSPCs on PDMS substrate with microscale stiffness patterns. (**A**) Migration trajectories of m-pSSPCs and l-pSSPCs on 20-μm and 50-μm stiffness-patterned substrates over 16 h. (**B**,**C**) Quantification of overall migration velocity (**B**) and migration efficiency (**C**) on 20-μm and 50-μm patterns. * $p < 0.05$, ** $p < 0.01$, *** $p < 0.001$, **** $p < 0.0001$.

3.4. 50-μm Stiffness Patterns Induce Morphological Polarization and Alignment in m-pSSPCs

Next, we analyzed cell morphology and orientation after 16 h of culture to assess whether the observed directional migration was accompanied by structure changes in the cells. On the 50-μm stiffness patterns, m-pSSPCs underwent profound morphological polarization (Figure 4A). The cells became smaller and elongated, evidenced by a significant increase in their aspect ratio (AR) and decrease in cellular area (Figure 4B,C), and their long axes aligned preferentially with the axis of the stiffness pattern (Figure 4A,E). In contrast, l-pSSPCs cultured on the 50-μm stiffness patterns maintained an isotropic morphology and orientation, without evident elongation or alignment (Figure 4A,E). This morphological response in m-pSSPCs was scale-dependent. When cultured on the 20-μm stiffness patterns, m-pSSPCs did not undergo polarization or alignment, instead displaying a random orientation similar to l-pSSPCs (Figure 4A,D). Overall, the morphological elongation and alignment of m-pSSPCs were observed exclusively on the 50-μm stiffness patterns.

Furthermore, we observed that m-pSSPCs specifically reinforce adhesions on the stiffer domains of the 50-μm pattern, evidenced by quantitative analysis of vinculin-positive focal adhesions. On the 50-μm patterned substrates, m-pSSPCs exhibited a significantly higher ($p < 0.01$) number and total area of focal adhesions on the stiff ridges than on the soft grooves (Figure S1A,B). In contrast, on the 20-μm patterns, such differences were no longer observed (Figure S1A,C).

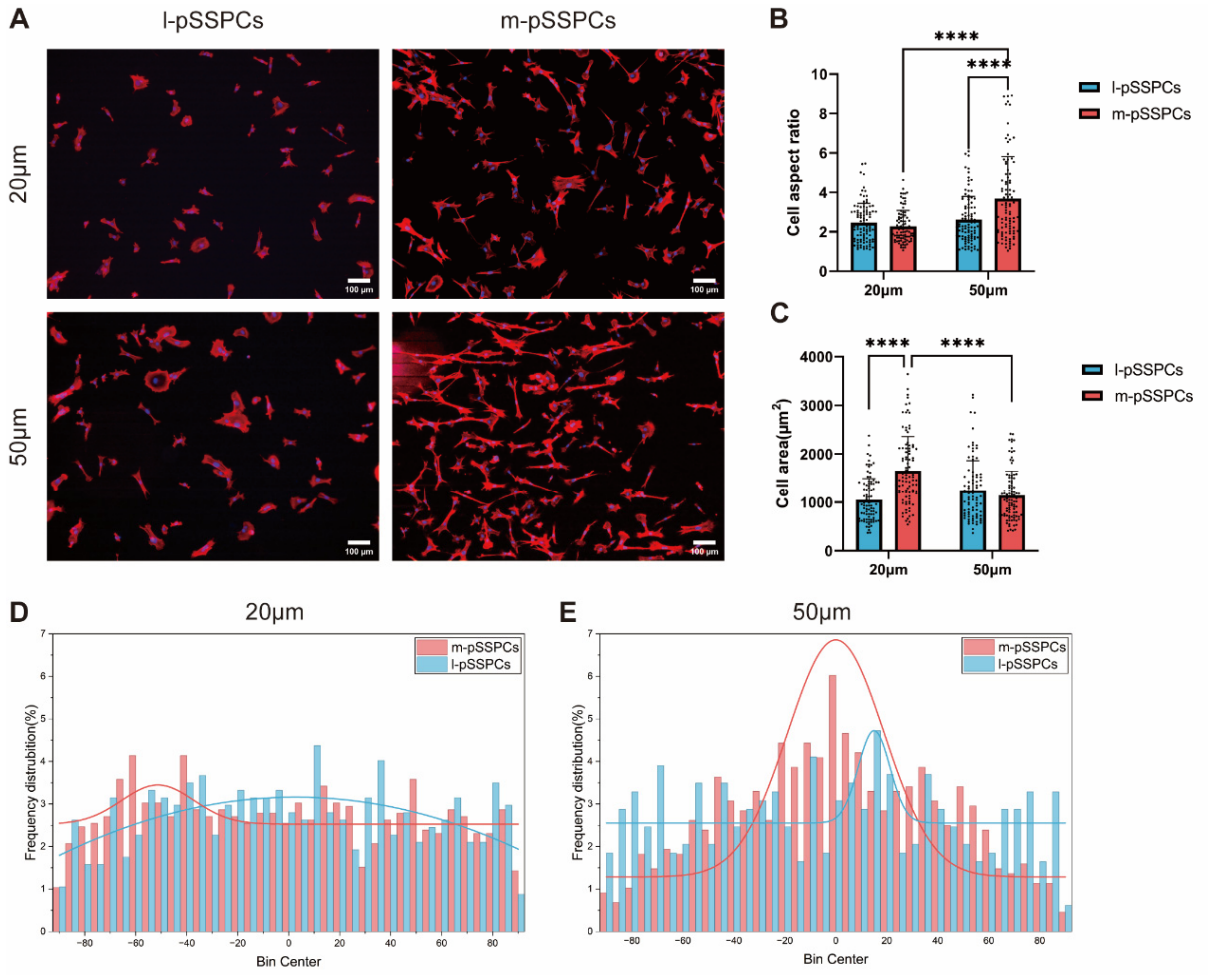

Figure 4. Morphological polarization and orientation of pSSPCs on stiffness-patterned substrates. (**A**) Representative images showing cell morphology and orientation of m-pSSPCs and l-pSSPCs on 20-μm and 50-μm stiffness-patterned substrates after 16 h. Scale bar, 100 μm. (**B**,**C**) Quantification of cell aspect ratio (**B**) and area (**C**) on 20-μm and 50-μm patterns. (**D**,**E**) Quantification of orientation angle distribution and directional alignment on 20-μm (**D**) and 50-μm (**E**) patterns. **** $p < 0.0001$.

3.5. Elevated Trpv2 Expression Is Required For Scale-Dependent Mechanosensitivity in m-pSSPCs

We performed bulk RNA sequencing to uncover the molecular basis for the divergent mechanosensitivity between m-pSSPCs and l-pSSPCs. Consistent with their similar baseline characteristics observed in vitro, the two cell types displayed transcriptional divergence. We identified 1963 significantly differentially expressed genes (DEGs)—a small fraction of the total transcriptome—with 769 upregulated and 1194 downregulated in m-pSSPCs relative to l-pSSPCs (Figure 5A, Table S2).

Despite the overall transcriptomic similarity, gene set enrichment analysis revealed a significant enrichment of calcium channel-related gene sets in m-pSSPCs (Figure 5B), suggesting a potential involvement of ion-channel-mediated mechanotransduction. A focused analysis of mechanosensitive and calcium-permeable ion channels showed that while most channels were similarly expressed, several candidates exhibited site-specific differences. Heatmap visualization highlighted *Trpv2*, *Trpc1*, and *Piezo1* as upregulated in m-pSSPCs, whereas *Trpv4* was downregulated (Figure 5C). Quantitative PCR further confirmed the significant upregulation of *Trpv2 in* m-pSSPCs. In contrast, no significant differences in *Piezo1* and *Trpv4* expression were observed between m-pSSPCs and l-pSSPCs (Figure 5D).

To test whether the elevated expression of *Trpv2* is required for the enhanced mechanosensitivity of m-pSSPCs, we knocked down its expression using specific siRNA, achieving an approximately 60% reduction in mRNA levels (Figure 5E). Strikingly, selective silencing of *Trpv2* completely abolished the characteristic response of m-pSSPCs to 50-μm stiffness patterns, losing their elongated morphology, adopting aspect ratios comparable to those of naive l-pSSPCs (Figure 5F). Furthermore, their directional alignment along the stiffness patterns was eliminated; their orientation distributions became random, rendering them indistinguishable from l-pSSPCs or from m-pSSPCs cultured on 20-μm patterns (Figure 5G,H).

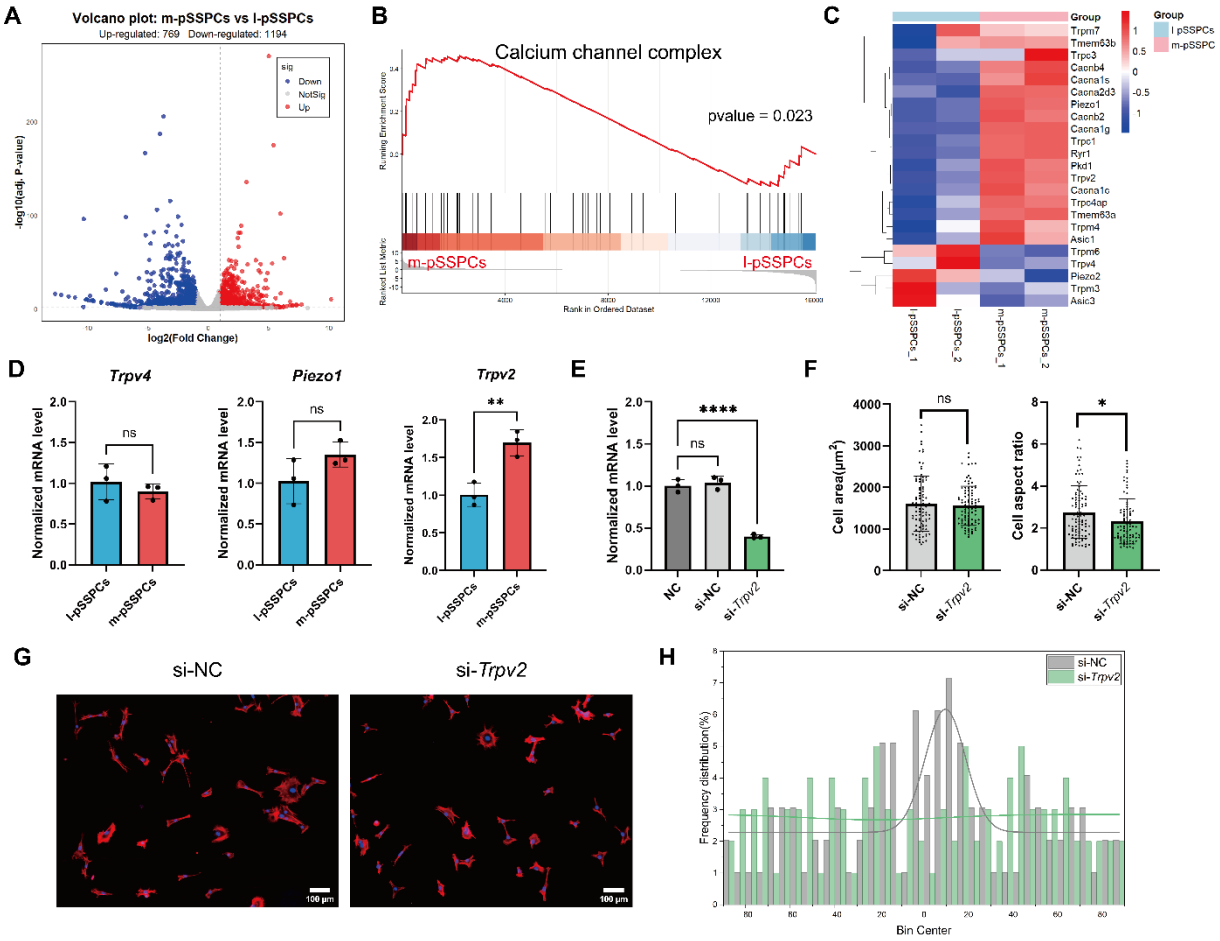

Figure 5. Transcriptomic analysis and functional validation of mechanosensitive ion channels in m-pSSPCs versus l-pSSPCs. (**A**) Volcano plot showing the DEGs in the bulk RNA-seq for m-pSSPCs and l-pSSPCs (passage 3, n = 2). Red, high expressed in m-pSSPCs; Blue, high expressed in l-pSSPCs. (**B**) GSEA analysis showing the enriched gene signature of 'GOCC_CALCIUM_CHANNEL_COMPLEX' in m-pSSPCs. (**C**) Heatmap of mechanosensitive and calcium-permeable ion channels. (D) The real-time qPCR quantification of *Trpv2*, *Piezo1*, and *Trpv4* expression in m-pSSPCs and l-pSSPCs (passage 3). (**E**) *Trpv2* knockdown efficiency by siRNA in m-pSSPCs. (**F**) Cell area and aspect ratios in si-NC and si-*Trpv2* treated m-pSSPCs on 50-μm patterns. (**G**) Representative images showing cell morphology and orientation in si-NC and si-*Trpv2* treated m-pSSPCs on 50-μm patterns. Scale bar, 100 μm. (**H**) Quantification of orientation angle distribution and directional alignment in si-NC and si-*Trpv2* treated m-pSSPCs on 50-μm patterns. * $p < 0.05$, ** $p < 0.01$, **** $p < 0.0001$.

4. Discussion

The clinical imperative to reconstruct maxillofacial defects calls for regenerative strategies that move beyond a "one-size-fits-all" approach toward a deeper understanding of site-specific skeletal stem cell biology [29]. In this study, we demonstrate that SSPCs derived from mandibular and lone bone periosteum, despite sharing similar cellular characteristics and largely overlapping transcriptomic profiles exhibit fundamentally distinct mechanosensory behaviors. By engineering a two-dimensional substrate with defined microscale stiffness patterns, we observed that m-pSSPCs selectively interpret a scale-dependent mechanosensing window (~0.5 MPa). This process depends on the elevated expression of the *Trpv2* calcium ion channel. Our findings demonstrated that SSPCs response to mechanical cues are influenced by their tissue or origin. Furthermore, our findings highlight the importance of considering site-specific properties in the design of biomaterials for craniofacial regeneration, where optimal outcomes may depend on aligning material cues with the intrinsic mechanosensing capabilities of target cell population.

In this study, we developed a bilayer PDMS substrates presents a uniform flat surface with defined periodic stiffness variation beneath by applying a soft top PDMS film (~9 μm, E ~ 899 kPa) over a micro-structured layer of stiff PDMS [23]. Over the rigid ridges, the film's deformation is constrained, yielding a high local apparent elastic modulus (*E_app*); over the grooves, the film can bend slightly, yielding a lower *E_app* [23,30]. This mechanical coupling generates the measured stiffness differential—~0.5 MPa on the 50-μm-stiffness patterns (2.4

MPa vs. 1.9 MPa) and ~0.3 MPa on the 20-μm patterns (2.4 MPa vs. 2.1 MPa). Unlike conventional approaches that rely on micropatterned or grooved substrates [30,31], our design allows to decouple further cellular response to stiffness patterning from topographic effects. Importantly, these apparent modulus values fall within the stiffness range reported for early fracture callus. For instance, granulation and connective tissues in the inflammatory phase of rats exhibit a Young's modulus of approximately 1 MPa, while cartilage in the repair phase reaches about 5 MPa, and the overall modulus of a mouse femoral callus at day 14 post-fracture has been measured at ~2.76 MPa [32,33]. Therefore, the mechanical microenvironment engineered on our substrates, including the ~0.5 MPa stiffness differential between stiff and soft regions, approximates the stiffness variations encountered by cells within early reparative callus. This physiological relevance supports the interpretation that the observed cell migration and morphological responses likely reflect behaviors that occuring during the initial phase of bone healing, when the tissue is still soft and mechanically heterogeneous.

It is well established that SSPCs tend to migrate along continuous stiffness gradients, known as durotaxis [14]. However, the cellular response to discrete stiffness periodicities at microscale level remains largely unexplored. In this study, we observed that m-pSSPCs cultured on substrates with a 50-μm stiffness patterns selectively displayed pronounced morphological polarization and directional migration. Moreover, on the 50-μm pattern, m-pSSPCs exhibited significantly more focal adhesions on the stiff ridges than on the soft grooves, whereas no such difference was observed on the 20-μm pattern. These findings suggest that m-pSSPCs can perceive the ~0.5 MPa stiffness differential on the 50-μm patterned substrates, and translate such microscale mechanical cue into spatially reinforced adhesion maturation on the stiff regions, a key mechanotransductive event that likely drives subsequent cytoskeletal polarization and directional migration.

Emerging evidence indicates that substrate strain energy mediates cellular responses to mechanical cues, influencing migration, adhesion, and cytoskeletal organization [34]. This strain energy-based framework probably explains the scale-dependent nature of our observation. From a biophysical point of view, the 50-μm patterned substrates with the measured stiffness differential of ~0.5 MPa translates into a well-defined length scale where a single m-pSSPCs (~30–50 μm in spread diameter) can simultaneously anchor adhesions on both "high strain energy" (stiff) and "low strain energy" (soft) domains. This energetic imbalance across the cell body may drive the maturation of focal adhesion on the hard stripe, and coordinate the final alignment of the actomyosin cytoskeleton along the pattern axis [35]. In contrast, the 20-μm pattern presents a stiffness change over a distance shorter than a typical cell length, causing the mechanical anisotropy to be spatially averaged. In sum, on focal adhesion data experimentally support the proposed mechanotransductive cascade, although full validation will require direct measurements of traction forces or calcium signaling.

The fact that m-pSSPCs, but not l- pSSPCs, can resolve the 50-μm energy landscape suggests that m-pSSPCs possess an intrinsically higher sensitivity to strain energy contrast—a site-specific property that may reflect their developmental origin and native mechanical environment [36–38]. From a developmental perspective, the m-pSSPCs, which are largely derived from neural crest [37,39], and may exhibit intrinsically migratory and exhibit heightened sensitivity to environmental cues [40].

In this study, we identified *Trpv2* as a critical contributor to the divergent mechanosensitivity between m-pSSPCs and l-pSSPCs. The TRP family including *Trpv2*, *Trpv4*, has been reported to sense and respond to mechanical stimuli through interactions with the cytoskeleton, lipid rafts, or membrane protein complexes [41,42]. It is well established that the activation of *Trpv2*, triggering Ca^{2+} signaling further affects cell migration, adhesion formation and actin cytoskeleton dynamics [43–45]. The higher basal expression of *Trpv2* in m-pSSPCs may effectively lower the threshold for mechanical signal initiation, enabling m-pSSPCs to detect microscale stiffness cues that are "invisible" to their long-bone counterparts. Selective *Trpv2* silencing markedly weakened the characteristic polarization and alignment of m-pSSPCs on 50-μm stiffness patterns, resulting in a morphology that closely resembles that of l-pSSPCs.

It is noted that several practical constraints should be noted when interpreting these results. First, downstream osteogenic differentiation was not assessed. Although qRT-PCR and immunofluorescence were initially considered, the small patterned area, low seeding density, and short culture period collectively yielded insufficient cell numbers and RNA quantity for reliable evaluation of osteogenic marker expression. Second, our mechanistic interpretation regarding *Trpv2* is based primarily on siRNA-mediated loss-of-function experiments. Pharmacological rescue with a TRPV2 agonist was not attempted because the candidate compound Probenecid has been reported to act as an allosteric potentiator rather than a direct channel opener [46]. Live-cell calcium imaging was also not feasible due to optical limitations imposed by the thick PDMS substrate. Complementary approaches such as improved pharmacological modulation and imaging-compatible platform adaptations (e.g., to enable live-cell Ca^{2+} readouts) will be valuable in future work to further refine the mechanistic sequence.

In summary, our study offers a proof-of-concept for the rational design of site-specific biomaterials. For oral and maxillofacial reconstruction, incorporating stiffness periodicities that match the intrinsic mechanosensing window of m-pSSPCs may enhance the recruitment, alignment, and tissue organization of endogenous progenitor cells within bone defects. More broadly, our results challenge the prevailing paradigm that skeletal progenitors from different anatomical sites can be treated as interchangeable for regenerative purposes, demonstrating instead that site of origin programs fundamental aspects of cellular mechanobiology.

5. Conclusions

In this study, we demonstrate that SSPCs derived from mandibular and lone bone periosteum, exhibit fundamentally distinct mechanosensory behaviors, despite sharing similar cellular characteristics and largely overlapping transcriptomic profiles. Specifically, Mandibular periosteum derived SSPCs exhibit a unique, scale-dependent sensitivity to 50-μm stiffness patterns (stiffness differential ~0.5 MPa)—a response mediated by the elevated expression of mechanosensitive ion channel *Trpv2*. These findings underscore that skeletal progenitors from different anatomical sites are not functionally interchangeable, which carries important implications for understanding basic bone biology and developing targeted regenerative therapies.

Supplementary Materials

The additional data and information can be downloaded at: https://media.sciltp.com/articles/others/2606151733508866/RMD-26040003-SM-final.zip. Figure S1: Focal adhesions of m-pSSPCs on 50 μm and 20 μm stiffness patterns. (A) Representative micrograph of immunofluorecent staining of Vinculin (green) of m pSSPCs on stiff (bright channel) and soft (dark channel) regions of 50 μm and 20 μm stiffness patterns. Scale bar, 20 μm. (B,C) Quantification of focal adhesion for m pSSPCs on 50 μm pattern (B) and 20 μm pattern (C), including number of focal adhesions per cell, total focal adhesion area per cell, and mean focal adhesion area per cell. ** $p < 0.01$; ns, not significant. Table S1: Primers used in this study. Table S2: DEGs upregulated in m-pSSPCs compared with l-pSSPCs.

Author Contributions

Q.L.: Writing—original draft, methodology, investigation, data curation; C.Z.: Writing—original draft, methodology, data curation; K.Z.: data curation; S.J.: investigation, data curation; L.X.: methodology, data curation; W.J.: Writing—review & editing, funding acquisition, conceptualization, supervision. All authors have read and agreed to the published version of the manuscript.

Funding

This work was financially supported by the Fundamental Research Funds for the Central Universities (2042024YXB018) and International Team of Implantology (ITI) Research Foundation (1721–2022).

Institutional Review Board Statement

The animal study was reviewed and approved by the Institutional Animal Care and Use Committee of Wuhan University (Approval No. WP20230204).

Informed Consent Statement

Not applicable. This study did not involve human subjects.

Data Availability Statement

The datasets used and/or analyzed during the current study are available from the corresponding author on reasonable request.

Acknowledgments

The authors thank the State Key Laboratory of Oral & Maxillofacial Reconstruction and Regeneration and the Core Facility of Wuhan University, for providing experimental facilities and technical assistance.

Conflicts of Interest

The authors declare no conflict of interest.

Use of AI and AI-Assisted Technologies

During the preparation of this work, the authors used Grammarly to improve grammar and syntax; no content of ideas were generated by AI. After using this tool, the authors reviewed and edited the content as needed and take full responsibility for the content of the published article.

References

1. Kumar, B.P.; Venkatesh, V.; Kumar, K.A.J.; et al. Mandibular Reconstruction: Overview. *J. Maxillofac. Oral Surg.* **2015**, *15*, 425–441. https://doi.org/10.1007/s12663-015-0766-5.
2. Momoh, A.O.; Yu, P.; Skoracki, R.J.; et al. A Prospective Cohort Study of Fibula Free Flap Donor-Site Morbidity in 157 Consecutive Patients. *Plast. Reconstr. Surg.* **2011**, *128*, 714–720. https://doi.org/10.1097/PRS.0b013e318221dc2a.
3. Dimitriou, R.; Mataliotakis, G.I.; Angoules, A.G.; et al. Complications following autologous bone graft harvesting from the iliac crest and using the RIA: A systematic review. *Injury* **2011**, *42*, S3-S15. https://doi.org/10.1016/j.injury.2011.06.015.
4. Wu, J.; Min, A.; Wang, W.; et al. Trends in the incidence, prevalence and years lived with disability of facial fracture at global, regional and national levels from 1990 to 2017. *PeerJ* **2021**, *9*, e10693. https://doi.org/10.7717/peerj.10693.
5. Bahney, C.S.; Zondervan, R.L.; Allison, P.; et al. Cellular biology of fracture healing. *J. Orthop. Res.* **2018**, *37*, 35–50. https://doi.org/10.1002/jor.24170.
6. Colnot, C. Skeletal Cell Fate Decisions Within Periosteum and Bone Marrow During Bone Regeneration. *J. Bone Miner. Res.* **2009**, *24*, 274–282. https://doi.org/10.1359/jbmr.081003.
7. Ortinau, L.C.; Wang, H.; Lei, K.; et al. Identification of Functionally Distinct Mx1+αSMA+ Periosteal Skeletal Stem Cells. *Cell Stem Cell* **2019**, *25*, 784–796.e5. https://doi.org/10.1016/j.stem.2019.11.003.
8. Liu, R.; Jiao, Y.-R.; Huang, M.; et al. Mechanosensitive protein polycystin-1 promotes periosteal stem/progenitor cells osteochondral differentiation in fracture healing. *Theranostics* **2024**, *14*, 2544–2559. https://doi.org/10.7150/thno.93269.
9. Dong, G.; Wang, J.; Chen, Z.; et al. Regulatory effects of stress release from decellularized periosteum on proliferation, migration, and osteogenic differentiation of periosteum-derived cells. *Biomater. Sci.* **2024**, *12*, 3360–3373. https://doi.org/10.1039/d4bm00358f.
10. Ghiasi, M.S.; Chen, J.; Vaziri, A.; et al. Bone fracture healing in mechanobiological modeling: A review of principles and methods. *Bone Rep.* **2017**, *6*, 87–100. https://doi.org/10.1016/j.bonr.2017.03.002.
11. Fu, X.; Liu, G.; Halim, A.; et al. Mesenchymal Stem Cell Migration and Tissue Repair. *Cells* **2019**, *8*, 784. https://doi.org/10.3390/cells8080784.
12. Lim, R.; Banerjee, A.; Biswas, R.; et al. Mechanotransduction through adhesion molecules: Emerging roles in regulating the stem cell niche. *Front. Cell Dev. Biol.* **2022**, *10*, 966662. https://doi.org/10.3389/fcell.2022.966662.
13. Putra, V.D.L.; Kilian, K.A.; Knothe Tate, M.L. Biomechanical, biophysical and biochemical modulators of cytoskeletal remodelling and emergent stem cell lineage commitment. *Commun. Biol.* **2023**, *6*, 75. https://doi.org/10.1038/s42003-022-04320-w.
14. Shellard, A.; Mayor, R. Collective durotaxis along a self-generated stiffness gradient *in vivo*. *Nature* **2021**, *600*, 690–694. https://doi.org/10.1038/s41586-021-04210-x.
15. Lewis, K.J. Osteocyte calcium signaling—A potential translator of mechanical load to mechanobiology. *Bone* **2021**, *153*, 116136. https://doi.org/10.1016/j.bone.2021.116136.
16. Qin, L.; He, T.; Chen, S.; et al. Roles of mechanosensitive channel Piezo1/2 proteins in skeleton and other tissues. *Bone Res.* **2021**, *9*, 44. https://doi.org/10.1038/s41413-021-00168-8.
17. Leucht, P.; Kim, J.-B.; Amasha, R.; et al. Embryonic origin and Hox status determine progenitor cell fate during adult bone regeneration. *Development* **2008**, *135*, 2845–2854. https://doi.org/10.1242/dev.023788.
18. Siyu, J.; Conghui, Z.; Wei, J. Single-cell Sequencing Resolves Heterogeneity in Mandible and Limb Bud Development. *J. Oral Sci. Res.* **2025**, *41*, 849–855. https://doi.org/10.13701/j.cnki.kqyxyj.2025.10.004.
19. Soares, A.P.; Fischer, H.; Aydin, S.; et al. Uncovering the unique characteristics of the mandible to improve clinical approaches to mandibular regeneration. *Front. Physiol.* **2023**, *14*. https://doi.org/10.3389/fphys.2023.1152301.
20. Zhu, D.; Tong, X.; Trinh, P.; et al. Mimicking Cartilage Tissue Zonal Organization by Engineering Tissue-Scale Gradient Hydrogels as 3D Cell Niche. *Tissue Eng. Part A* **2017**, *24*, 1–10. https://doi.org/10.1089/ten.tea.2016.0453.
21. Zhang, S.; Zhu, J.; Jin, S.; et al. Jawbone periosteum-derived cells with high osteogenic potential controlled by R-spondin 3. *FASEB J.* **2024**, *38*, e70079. https://doi.org/10.1096/fj.202400988RR.
22. Chan, C.K.; Seo, E.Y.; Chen, J.Y.; et al. Identification and Specification of the Mouse Skeletal Stem Cell. *Cell* **2015**, *160*, 285–298. https://doi.org/10.1016/j.cell.2014.12.002.
23. Lin, Q.; Zhang, K.; Jin, S.; et al. Microfabrication of Substrates with Microscale Stiffness Gradients to Guide Bone Marrow Stromal Cell Migration. *J. Vis. Exp.* **2025**, *225*, e69473. https://doi.org/10.3791/69473.
24. Gorelik, R.; Gautreau, A. Quantitative and unbiased analysis of directional persistence in cell migration. *Nat. Protoc.*

2014, *9*, 1931–1943. https://doi.org/10.1038/nprot.2014.131.
25. Horzum, U.; Ozdil, B.; Pesen-Okvur, D. Step-by-step quantitative analysis of focal adhesions. *MethodsX* **2014**, *1*, 56–59. https://doi.org/10.1016/j.mex.2014.06.004.
26. Langmead, B.; Salzberg, S.L. Fast gapped-read alignment with Bowtie 2. *Nat. Methods* **2012**, *9*, 357–359. https://doi.org/10.1038/nmeth.1923.
27. Li, B.; Dewey, C.N. RSEM: Accurate transcript quantification from RNA-Seq data with or without a reference genome. *BMC Bioinform.* **2011**, *12*, 323. https://doi.org/10.1186/1471-2105-12-323.
28. Love, M.I.; Huber, W.; Anders, S. Moderated estimation of fold change and dispersion for RNA-seq data with DESeq2. *Genome Biol.* **2014**, *15*, 550. https://doi.org/10.1186/s13059-014-0550-8.
29. Ambrosi, T.H.; Taheri, S.; Chen, K.; et al. Human skeletal development and regeneration are shaped by functional diversity of stem cells across skeletal sites. *Cell Stem Cell* **2025**, *32*, 811–823.e11. https://doi.org/10.1016/j.stem.2025.02.013.
30. Pham, J.T.; Xue, L.; del Campo, A.; et al. Guiding cell migration with microscale stiffness patterns and undulated surfaces. *Acta Biomater.* **2016**, *38*, 106–115. https://doi.org/10.1016/j.actbio.2016.04.031.
31. Nikkhah, M.; Edalat, F.; Manoucheri, S.; et al. Engineering microscale topographies to control the cell–substrate interface. *Biomaterials* **2012**, *33*, 5230–5246. https://doi.org/10.1016/j.biomaterials.2012.03.079.
32. Aegerter, C.M.; Wehner, T.; Steiner, M.; et al. Prediction of the Time Course of Callus Stiffness as a Function of Mechanical Parameters in Experimental Rat Fracture Healing Studies—A Numerical Study. *PLoS ONE* **2014**, *9*, e115695. https://doi.org/10.1371/journal.pone.0115695.
33. Miga, M.I.; Weis, J.A.; Granero-Molto, F.; et al. Quantifying Mechanical Properties in a Murine Fracture Healing System Using an Inverse Geometric Nonlinear Elasticity Modeling Framework. In *International Symposium on Biomedical Simulation*; Springer: Berlin/Heidelberg, Germany, 2010.
34. Panzetta, V.; Fusco, S.; Netti, P.A. Cell mechanosensing is regulated by substrate strain energy rather than stiffness. *Proc. Natl. Acad. Sci.USA* **2019**, *116*, 22004–22013. https://doi.org/10.1073/pnas.1904660116.
35. Prager-Khoutorsky, M.; Lichtenstein, A.; Krishnan, R.; et al. Fibroblast polarization is a matrix-rigidity-dependent process controlled by focal adhesion mechanosensing. *Nat. Cell Biol.* **2011**, *13*, 1457–1465. https://doi.org/10.1038/ncb2370.
36. Aghaloo, T.L.; Chaichanasakul, T.; Bezouglaia, O.; et al. Osteogenic Potential of Mandibular vs. Long-bone Marrow Stromal Cells. *J. Dent. Res.* **2010**, *89*, 1293–1298. https://doi.org/10.1177/0022034510378427.
37. Ichikawa, Y.; Watahiki, J.; Nampo, T.; et al. Differences in the developmental origins of the periosteum may influence bone healing. *J. Periodontal Res.* **2014**, *50*, 468–478. https://doi.org/10.1111/jre.12229.
38. Li, L.; Liu, Y.; Qian, X.; et al. Modulating the phenotype and function of bone marrow-derived macrophages via mandible and femur osteoblasts. *Int. Immunopharmacol.* **2024**, *132*. https://doi.org/10.1016/j.intimp.2024.112000.
39. Galea, G.L.; Zein, M.R.; Allen, S.; et al. Making and shaping endochondral and intramembranous bones. *Dev. Dyn.* **2020**, *250*, 414–449. https://doi.org/10.1002/dvdy.278.
40. Goodwin, K.; Nelson, C.M. Mechanics of Development. *Dev. Cell* **2021**, *56*, 240–250. https://doi.org/10.1016/j.devcel.2020.11.025.
41. Christensen, A.P.; Corey, D.P. TRP channels in mechanosensation: Direct or indirect activation? *Nat. Rev. Neurosci.* **2007**, *8*, 510–521. https://doi.org/10.1038/nrn2149.
42. Eijkelkamp, N.; Quick, K.; Wood, J.N. Transient Receptor Potential Channels and Mechanosensation. *Annu. Rev. Neurosci.* **2013**, *36*, 519–546. https://doi.org/10.1146/annurev-neuro-062012-170412.
43. Kyprianou, N.; Oulidi, A.; Bokhobza, A.; et al. TRPV2 Mediates Adrenomedullin Stimulation of Prostate and Urothelial Cancer Cell Adhesion, Migration and Invasion. *PLoS ONE* **2013**, *8*, e64885. https://doi.org/10.1371/journal.pone.0064885.
44. Schwab, A.; Fabian, A.; Hanley, P.J.; et al. Role of Ion Channels and Transporters in Cell Migration. *Physiol. Rev.* **2012**, *92*, 1865–1913. https://doi.org/10.1152/physrev.00018.2011.
45. Wei, C.; Wang, X.; Zheng, M.; et al. Calcium gradients underlying cell migration. *Curr. Opin. Cell Biol.* **2012**, *24*, 254–261. https://doi.org/10.1016/j.ceb.2011.12.002.
46. Rocereta, J.A.; Sturhahn, T.; Pumroy, R.A.; et al. Structural insights into TRPV2 modulation by probenecid. *Nat. Struct. Mol. Biol.* **2025**, *32*, 1019–1029. https://doi.org/10.1038/s41594-025-01494-9.